The synaptic tag as an emergent biophysical state depending on the synaptic actin network and the postsynaptic density

Francesco Negri[1,2†], Jannik Luboeinski[1,2,3†], Christian Tetzlaff[1,3], Michael Fauth[1,2*]

[1]III. Institute for Physics – Biophysics, Georg August University, Göttingen, Germany.
[2]Bernstein Center for Computational Neuroscience, Georg August University, Göttingen, Germany.
[3]Department for Neuro- and Sensory Physiology, University of Göttingen Medical Center, Göttingen, Germany.

*Corresponding author(s). E-mail(s): mfauth@gwdg.de;
†These authors contributed equally to this work.

Abstract

According to the synaptic tagging-and-capture hypothesis, long-term synaptic plasticity requires postsynaptic sites to establish a synaptic tag, enabling them to capture plasticity-related products synthesized elsewhere in the neuron. Although electrophysiological studies have provided evidence for the existence of synaptic tags, it remains largely unresolved which biophysical processes or synaptic molecules or properties implement them. In this study, we examine the hypothesis that a mismatch between dendritic spine volume and the size of the postsynaptic density (PSD) inheres the essential characteristics of a synaptic tag. To test this hypothesis, we developed a computational model that integrates established principles of calcium-dependent synaptic plasticity with the complex biochemical dynamics of actin, which is a key structural protein determining dendritic spine geometry. Using this model, we demonstrate the plausibility of our hypothesis by showing that the model can reproduce and explain a broad range of experimental findings across diverse synaptic plasticity protocols at the level of individual synapses as well as heterosynaptic plasticity protocols involving two synapses. Furthermore, the model predicts that the repeated induction of plasticity within a one-hour time window results in a nonlinear accumulation of synaptic changes, reminiscent of the spacing effect observed in psychological studies of learning and

memory. These results offer a concise mechanistic framework for understanding critical synaptic processes and suggest how temporal disparities in structural and biochemical dynamics can form a memory trace that could act as a synaptic tag.

Keywords: synaptic plasticity, consolidation, tagging and capture, model

Introduction

Synapses and their adaptation through synaptic plasticity are associated to the mechanisms of learning and memory [1]. The most prominent forms of synaptic plasticity are long-term potentiation (LTP, [2]) and long-term depression (LTD, [3]). Both have been found to undergo at least two major phases [4]: an early phase, decaying after a few hours, and a late phase that persists for several hours or even days. According to the *synaptic tagging-and-capture hypothesis*, the late phase only occurs if two factors are present at the same time at the (post)synapse [5, 6]: (i) plasticity-related products (PRPs) such as *de novo* synthesized proteins that can be captured by the synapse, and (ii) a so-called synaptic tag that indicates whether the synapse has received plasticity-triggering stimulation. The presence of the synaptic tag at the synapse then leads to the capture of PRPs. Note that both factors are present independently of each other, as a synaptic tag can be set without explicitly triggering PRP synthesis [5] or a tagged synapse can express late-phase plasticity by capturing PRPs that are being synthesized in response the stimulation of other synapses [7–10]. While numerous studies have investigated the trafficking, synthesis and turnover of plasticity-related proteins [11**?** –13], the synaptic tag still remains a mystery. Despite experimental evidence suggesting that the synaptic tag is unlikely to consist of a single type of molecule [14] and instead reflects a transient structural state of the synapse [6], the specific biochemical or biophysical processes that form the synaptic tag are still unknown.

Most computational models characterizing the processes of the synaptic-tagging-and-capture hypothesis are phenomenological [15–20], usually describing the synaptic tag as abstract variable that depends on the early-phase of synaptic plasticity. In this study, drawing from previous theoretical models [19, 21, 22], we develop a new tagging-and-capture model that captures the dynamic changes of the volume of the postsynaptic spine, which is based on the different dynamic states of the structural protein actin as well as of the postsynaptic density (PSD). Using this model, we test the hypothesis that a mismatch between actin-dependent spine volume and the PSD could represent the synaptic tag.

Actin is a globular protein that forms filaments. These preferentially polymerize at one end and depolymerize at the other, resulting in a continuous treadmilling. When close to the membrane, this induces pushing forces and retrograde movement of the filament [23], which continuously alters the spine shape [21, 22, 24, 25]. Additionally, multiple actin-binding proteins, such as the branching protein complex ARP2/3 or the severing protein cofilin, organize the filaments into continuously growing and reorganizing, branched networks. On the other hand, crosslinking proteins such as drebrin, actinin or CaMKIIβ [26, 27] can bind to the filaments, slowing down treadmilling and

reorganization. This gives rise to at least two main populations of actin, exhibiting different treadmilling speeds [28], which we refer to as the *dynamic* and the *stable actin pool*. Typically, the activity of the dynamic actin pool is localized to discrete polymerization foci at the tip of the spine [29], where an increased retrograde movement of filaments is observed, whereas the stable actin pool forms a crosslinked mass at the bottom of the spine [28]. Following a plasticity-inducing stimulation, the concentrations as well as the reaction rates of actin-binding proteins in the spine undergo changes [27, 30]. While these changes are not long-lasting, they give rise to a rapid remodeling of spine geometry and alterations in the stable and dynamic actin pools [21, 25, 31, 32], which may persist on timescales of hours [21, 33].

To relate the dynamics of actin and the spine volume to long-lasting plasticity of the synaptic transmission efficacy, we focus on the dynamical behavior of the PSD. The PSD size (as measured by fluorescence or electron microscopy) is strongly correlated with the synaptic transmission efficacy (e.g., as measured by EPSPs [34]) through the number of AMPA receptors anchored at the postsynaptic site. In particular, it has been postulated that depending on its size, the PSD provides a number of slots for AMPA receptors [6, 35]. Moreover, in the basal state, the PSD size is correlated with the spine volume [36, 37], and previous modeling has shown that the PSD size determines the the stationary volume around which a spine fluctuates [22]. This correlation is transiently disturbed during a plasticity event due to the aforementioned changes in actin and spine geometry. However, it is reestablished on a timescale of minutes to hours by adapting the PSD size to the new spine volume [37, 38], which is consistent with the timescale of PRP capture [5, 6, 39]. Thus, in other words, our hypothesis implies that the PSD is able to react to changes in actin-dependent spine volume and, when free PRPs are available in the spine, adapt its size to match the new spine volume.

In this study, we test the viability of our hypothesis using a mathematical model of actin-dependent volume dynamics and its interplay with PSD changes. After providing a detailed description of the core principles of the actin-PSD model, we first show in a proof-of-concept setup that the temporal development of the different biochemical and -physical processes can account for the formation of a synaptic tag on the experimentally observed timescale. Next, integrating the actin-PSD model with a more detailed model of calcium-dependent plasticity, we demonstrate the validity of our hypothesis under biologically more detailed conditions. Further, we show for both versions of the model that the hypothesis also applies to multi-synaptic protocols, and that it can further provide new predictions about the synaptic dynamics given sequential stimulation protocols.

Results

Model for late-phase plasticity

Our proof-of-concept actin-PSD model (see Fig. 1) is based on recent insights that the spine volume results from the overall amount of actin filaments in a dynamic and a stable pool [21]. Here, we simplify the complex interplay between these two actin pools and the spine geometry by directly considering that the total spine volume V_{tot} is the sum of volumes resulting from the dynamic actin pool V_{d} and the stable actin

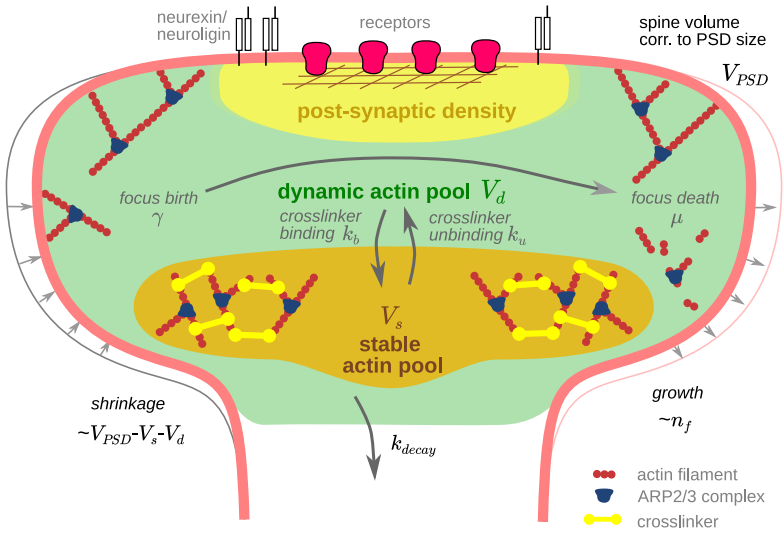

Fig. 1 Sketch of the main quantities and processes in the actin-PSD model. The formation of foci leads to the generation of new actin filaments. These actin filaments are contained either in the dynamic or in the stable pool and can transition between these pools by binding and unbinding of crosslinkers.

pool V_s. On the other hand, experiments show that there is a correlation between the spine volume and the size of the corresponding PSD [36, 37], and biophysical models demonstrate that a certain PSD size entails a certain spine volume even in the absence of actin [22, 25]. Therefore, we consider here a volume V_PSD to model the PSD size, which allows us to mathematically relate and compare it to the different actin volumes. In the following, we will describe the core biochemical and -physical processes influencing the dynamics of these different spine-related volumes.

The temporal evolution of the volume resulting from the dynamic actin pool is determined by (i) the continuous transition of actin between dynamic and stable state due to crosslinker binding and unbinding, (ii) the formation of new actin filaments dependent on the number of polymerization foci, and (iii) counteracting forces from the cell membrane (cf. Eq. 1 in Methods):

$$\frac{dV_\mathrm{d}}{dt} = -k_\mathrm{b}(t)V_\mathrm{d} + k_\mathrm{u}(t)V_\mathrm{s} + k_\mathrm{growth} \cdot n_\mathrm{f}(t) - k_\mathrm{decay}\left[\frac{V_\mathrm{d}}{V_\mathrm{d}+V_\mathrm{s}} - c_0\right]_+ [V_\mathrm{d}+V_\mathrm{s}-V_\mathrm{PSD}]_+ \,.$$

The first two terms on the right-hand side cover exchange between the stable and the dynamic pool determined by crosslinker binding with rate $k_\mathrm{b}(t)$ and unbinding with rate $k_\mathrm{u}(t)$. These rates are usually constant, but may change upon stimulation [26, 27]. In general, the polymerization of new actin filaments happens in distinct polymerization foci [29], which are formed and dissolved stochastically [22]. We therefore describe the number of foci n_f, which determines the third term on the right-hand side, by a birth-death process with birth rate $\gamma(t)$ and death rate $\mu(t)$. Finally, the fourth term

describes the mismatch between actin and PSD-dependent volumes: If the total synaptic volume $V_{\mathrm{tot}} = V_{\mathrm{d}} + V_{\mathrm{s}}$ is larger than the volume corresponding to the PSD size V_{PSD}, the membrane exerts counteracting forces. These forces hinder actin polymerization or push material out of the spine, leading to a net reduction in the dynamic actin pool and the related volume V_{d} with rate k_{decay}. Thus, the dynamic pool shrinkage is considered to be proportional to the difference between actin and PSD volume (as long as it is positive). If there is a larger dynamic actin volume, this effect will be stronger. Hence, the above described volume-dependent shrinkage is scaled by a factor that describes by how much the fraction of dynamic actin exceeds an offset concentration c_0.

The evolution of the spine volume that results from the stable pool is fully described by the continuous exchange of actin between the stable and the dynamic pool (cf. Eq. 2 in Methods):

$$\frac{dV_{\mathrm{s}}}{dt} = +k_{\mathrm{b}}(t)V_{\mathrm{d}} - k_{\mathrm{u}}(t)V_{\mathrm{s}}.$$

The dynamics of the PSD, and hence of V_{PSD}, is gated by the availability or concentration of PRPs, represented by $\phi(t)$, and it will only change if the current spine volume V_{tot}, resulting from the actin-dynamics, is not in equilibrium with the PSD-dependent volume. The temporal evolution is therefore given by (cf. Eq. 3 in Methods):

$$\frac{dV_{\mathrm{PSD}}}{dt} = \phi(t) \cdot f_{\mathrm{int}} \cdot \left[\underbrace{V_{\mathrm{d}} + V_{\mathrm{s}}}_{V_{\mathrm{tot}}} - \underbrace{(V_{\mathrm{PSD}} + V_n^*)}_{V_{\mathrm{tot}}^{\mathrm{PSD}}} \right] / \tau_{\mathrm{PSD}}.$$

Here, $V_{\mathrm{tot}}^{\mathrm{PSD}}$ is the total spine volume expected for the current PSD size given the stochastic polymerization of actin filaments ($n_{\mathrm{f}}(t)$), which leads to the correction factor $V_n^* \neq 0$ (see Methods). The factor f_{int} accounts for the physical scaling of the integration of PRPs into the PSD. It can be seen that when PRP is available ($\phi = 1$), the volume corresponding to the PSD size will evolve to reestablish the equilibrium with the actin-induced volume. Thus, given our hypothesis that the temporal difference between actin-dependent spine volume and PSD size could represent the synaptic tag, we define in the following the synaptic tag as $V_{\mathrm{tot}} - V_{\mathrm{tot}}^{\mathrm{PSD}}$.

In the following, we show (1) how this tag can be set by modulation of actin dynamics, (2) how such modulations are induced by neural activity, (3) that the tag can account for heterosynaptic plasticity and that it decays on a similar timescale as observed in experiments, and (4) that our tag model can explain and predict the temporal interaction of multiple stimuli at the same synapse.

Setting the tag by modulation of actin dynamics

As a first step, we show that stimulus-induced changes in actin dynamics in our actin-PSD model can lead to the formation of a synaptic tag, which results in synaptic dynamics comparable to experimental findings. To this end, we test how our late-phase plasticity model behaves under standard plasticity-inducing stimuli, i.e., tetanus stimuli that induce LTP, and low-frequency stimuli (LFS) that induce LTD (cf. [39]). We

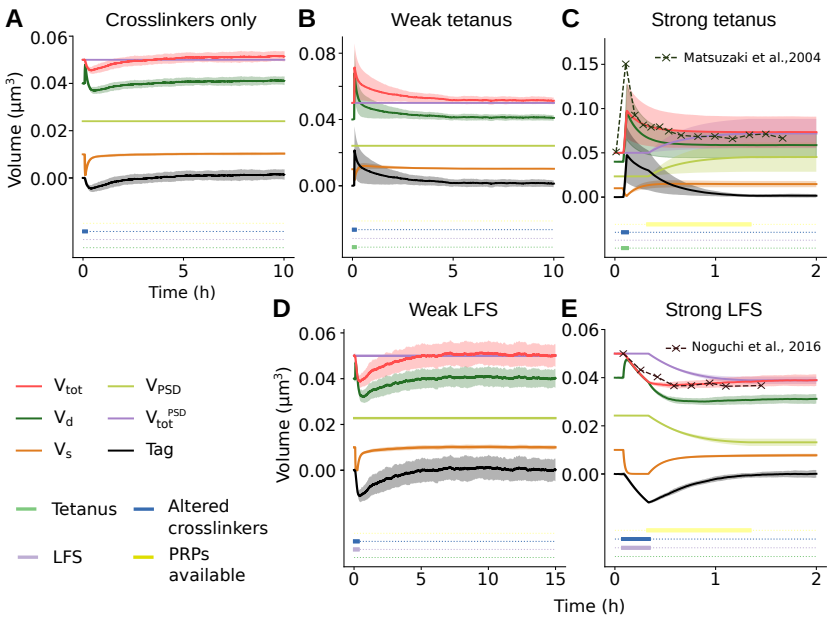

Fig. 2 The dynamics of the proof-of-concept model given standard LTP and LTD protocols. Time evolution of the hypothesized synaptic tag (black), the dynamic and stable actin volume, the PSD volume V_{PSD}, and derived quantities ($V_{\mathrm{tot}} = V_{\mathrm{d}} + V_{\mathrm{s}}$ and $V_{\mathrm{tot}}^{\mathrm{PSD}}$) over time under different conditions: (A) Plasticity-related alteration of crosslinker (un)binding (interval indicated by dark blue bar at bottom); (B) a weak tetanus (green bar) without PRP synthesis; (C) strong tetanus with PRP synthesis (yellow bar); (D) low-frequency stimulation (purple bar) without PRP synthesis and (E) with PRP synthesis. See Methods for details on the used stimuli. Dashed lines in panels C and E mark experimental results from [40] and [41].

model the influence of these stimuli directly by changing the parameters governing the actin dynamics. Thus, we switch from the basal actin parameter values to plasticity-related values during stimulation and back to the basal values after stimulation (see Methods and bottom of panels in Figs. 2-5 for the respective time intervals). In particular, the following parameters of the actin dynamics are changed (see Table 2): First, it is known that during LTP, crosslinkers rapidly unbind from the actin filaments, filaments are severed, and new actin foci emerge [27]. Similarly, also during LTD, crosslinker dynamics are altered [42, 43]. In our model, this is reflected by a change in the crosslinker binding and unbinding rates k_{b} and k_{u}. Second, the influx of calcium during both LTD and LTP triggers multiple signaling chains, which regulate, inter alia, the actin severing protein cofilin [44]. This can lead to increased severing and thus death of actin polymerization foci, but also to a large concentration of free actin monomers and nucleation of new filaments. Thus, in the model, we vary birth and death rates of actin foci accordingly, resulting in changes of n_{f}.

To assess the influence of individual parameter changes, we first tested what would happen if only the crosslinker binding and unbinding rates (k_{b}, k_{u}) are transiently altered (Fig. 2A). As expected, we found that this leads to a rapid transfer of actin from stable (ocher curve) to dynamic pool (dark green curve) and the subsequent

slow restoration of the stable pool to its stationary value, whereas the total volume of the actin pools only is transiently lowered and then quickly returns approximately to the basal level (pink curve). As the PSD volume does not change, the proposed synaptic tag (black curve) mirrors this behavior. Hence, altered crosslinkers alone will not induce long-term plasticity.

On the other hand, when the crosslinker dynamics (k_b, k_u) are altered and the birth rate of new foci (γ) is increased in parallel (Fig. 2B), which corresponds to a weak tetanization in experiments, an increase in the total volume is elicited. As compared to the case with crosslinkers only, we first observe an even stronger increase of the dynamic pool, which induces a slight and transient increase of the stable pool above its stationary level after the crosslinkers return to their normal rates. However, without PRP synthesis all quantities ultimately return to their initial (stationary) values and the proposed tag (black) decays. This is because the decay term in V_d drives the total volume of actin towards the volume determined by the PSD size V_PSD. However, once an increase in PRP synthesis is present (as during strong tetanization), V_PSD and, thus, $V_\mathrm{tot}^\mathrm{PSD}$ become dynamic and adapt to the perturbed total actin volume (Fig. 2C, violet and ocher). This leads to an accelerated decay of the proposed synaptic tag. As soon as $V_\mathrm{tot}^\mathrm{PSD}$ reaches the total actin volume, no further change happens, and the volume modifications become permanent. Note that in the presence of active PRP synthesis the resulting stable state $V_\mathrm{tot}^\mathrm{PSD} = V_\mathrm{d} + V_\mathrm{s}$ is a line attractor, which enables the total volume to take values from a continuous range (cf. Appendix). Further note that the parameter values were chosen such that the time course of V_tot resembles the relative volume changes from LTP-inducing glutamate uncaging experiments ([40], black dashed line in Fig. 2C).

Similar to the workings of LTP, our model can also account for LTD. Following experimental data, LTD yields the unbinding of crosslinkers, but in contrast to LTP the birth rate of new foci is decreased. These two changes together lead to a smaller increase in the dynamic pool volume upon stimulation and a decrease in the total actin volume, as well as a negative synaptic tag (Fig. 2D-E). When no PRP synthesis occurs, the total volume starts to increase again as soon as the stimulus ends and the birth rate of new foci is restored until the pre-stimulus level is reached (Fig. 2D). Once PRP synthesis is increased, the negative value of the tag causes a gradual decrease in V_PSD, which in turn removes the tag (Fig. 2E). Note that parameter values have been chosen such that the model matches the time course of spine volumes after low-frequency stimulation observed in experiments (dashed line, [41]).

In summary, the proposed actin-PSD model can express both early and late LTP as well as early and late LTD and reproduces the respective experiments using one and the same parameter set. This indicates that the difference between actin-dependent spine volume and PSD size sets a synaptic tag such that synaptic changes can be consolidated into long-lasting plasticity.

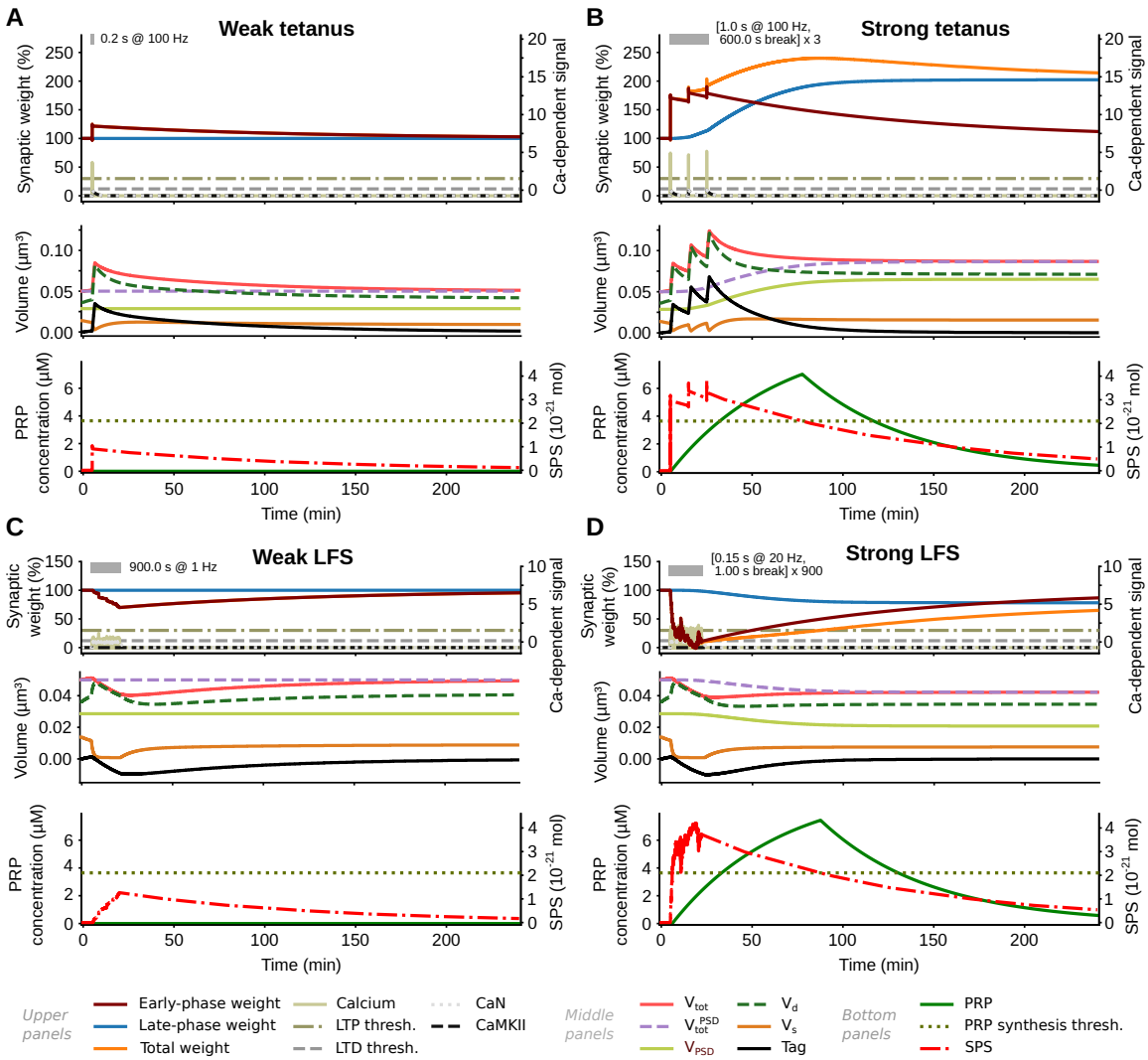

Fig. 3 Temporal evolution of synaptic weights and relevant quantities in the full-integrated, calcium-based model under different stimulation protocols. Stimulation is conveyed by presynaptic spike activity. (A) Weak tetanization leads to e-LTP, (B) strong tetanization induces l-LTP, (C) weak low-frequency stimulation induces e-LTD, and (D) strong low-frequency stimulation yields l-LTD.

Upper panels: Early-phase (brown, shifted for visualization purposes), late-phase (blue), and total weight (orange) of the individual synapse as well as calcium-dependent signals (calcium amount, CaN activity, and CaMKII activity, in normalized units). LTD and LTP thresholds are shown by dashed and dash-dot horizontal lines; CaMKII threshold $\theta_{\mathrm{CaMKII}} = 5$ not shown. Gray bar at the top: information on the time point, duration, and structure of the stimulation.

Middle panels: Quantities of late-phase plasticity of the individual synapse (dynamic pool: dark green dashed, stable pool: ocher, total volume: pink, PSD volume: light green, $V_{\mathrm{tot}}^{\mathrm{PSD}}$: purple dashed; compare Fig. 2).

Bottom panels: Quantities of neuron-wide processes – concentration of available PRP (dark green) and amount of the signal triggering PRP synthesis (SPS, red).

Integration with calcium-based early-phase plasticity and synthesis of plasticity-related products (PRPs)

As a next step, we investigate how the above described modulations in actin dynamics directly interact with pre- and postsynaptic spiking activity, calcium-dependent plasticity, and PRP synthesis dynamics. For this, we integrate our actin-PSD model with a calcium-based early-phase plasticity model (cf. [45]) and a PRP synthesis model (cf. [15]), which are well established from earlier studies on synaptic tagging and capture (see [15, 17–19]). We refer to this in the following as the "full-integrated model". This model comprises a weight component for early-phase plasticity that undergoes LTD when the calcium amount exceeds a threshold value θ_{d}, and LTP when calcium exceeds an even higher threshold θ_{p}. Otherwise the early weight decays towards its baseline value zero. PRP synthesis takes place when the deviation from the baseline, summed over all synapses of a neuron (referred to as "signal triggering PRP synthesis", SPS, cf. Eq. 6) exceeds a threshold θ_{ϕ}.

In the full-integrated model, our actin-PSD late-phase plasticity model is also coupled to neuronal activity, assuming that the calcium level at the postsynaptic site determines the crosslinker activity and the dynamics of actin foci. When calcium is above the LTD threshold θ_{d}, the signaling chain for depression is activated. We here assume calcineurin (CaN, [44, 46]) as a representative of this signaling chain and include a calcineurin signal that activates when calcium is above that threshold. The signal remains activated for a certain time afterward and as long as it is active, the above described effects of the LFS on the late-phase model are applied. Similarly, for tetanic stimulation and LTP, we model a CaMKII signal that triggers the proposed effects of tetanic stimulation on the late-phase model. This signal is activated when calcium exceeds an even higher threshold θ_{CaMKII}.

Given the direct relation between the PSD size, corresponding to V_{PSD}, and the number of AMPARs, we assume that the late-phase weight z is a linear function of V_{PSD} (cf. Eq. 8). This late-phase weight is added to the early-phase weight h to yield the total weight of the synapse as $w(t) = h(t) + z(t)$.

Using this model together with leaky integrate-and-fire neurons, we could induce plasticity via a presynaptic spiking activity resembling the stimulation used in classical tagging-and-capture experiments (cf. [39]; see Methods), similar as for the simple switching of the rate parameters in our late-phase-only model earlier.

During a weak tetanus (Fig. 3A), calcium rises above the thresholds for early LTP and CaMKII activation. This leads to similar actin dynamics as in Figure 2B. The induced plastic changes are, however, not large enough for the SPS signal to cross the threshold for PRP synthesis (Fig. 3A bottom), such that all quantities decay to their initial values. The strong tetanus (Fig. 3B), which consists of three prolonged stimulation intervals of the same high frequency, leads to more early LTP and thereby triggers PRP synthesis. Also, the total actin-dependent volume shows a temporal summation of changes from multiple stimulations, which are then resulting in an increase of V_{PSD}.

For low-frequency stimulation (Fig. 3C and D), we obtain calcium levels above the depression threshold but below the potentiation and CaMKII thresholds. Thus, actin nucleation is decreased and the overall actin-induced spine volume decays. For strong

low-frequency stimulation, enough early-phase plasticity is expressed to trigger PRP synthesis, such that V_{PSD} decreases.

Thus, in summary, our results show that the difference between actin-dependent spine volume and PSD size also serves as synaptic tag in a biologically more detailed computational model under different experimentally inspired neuronal stimulation protocols, further supporting our hypothesis.

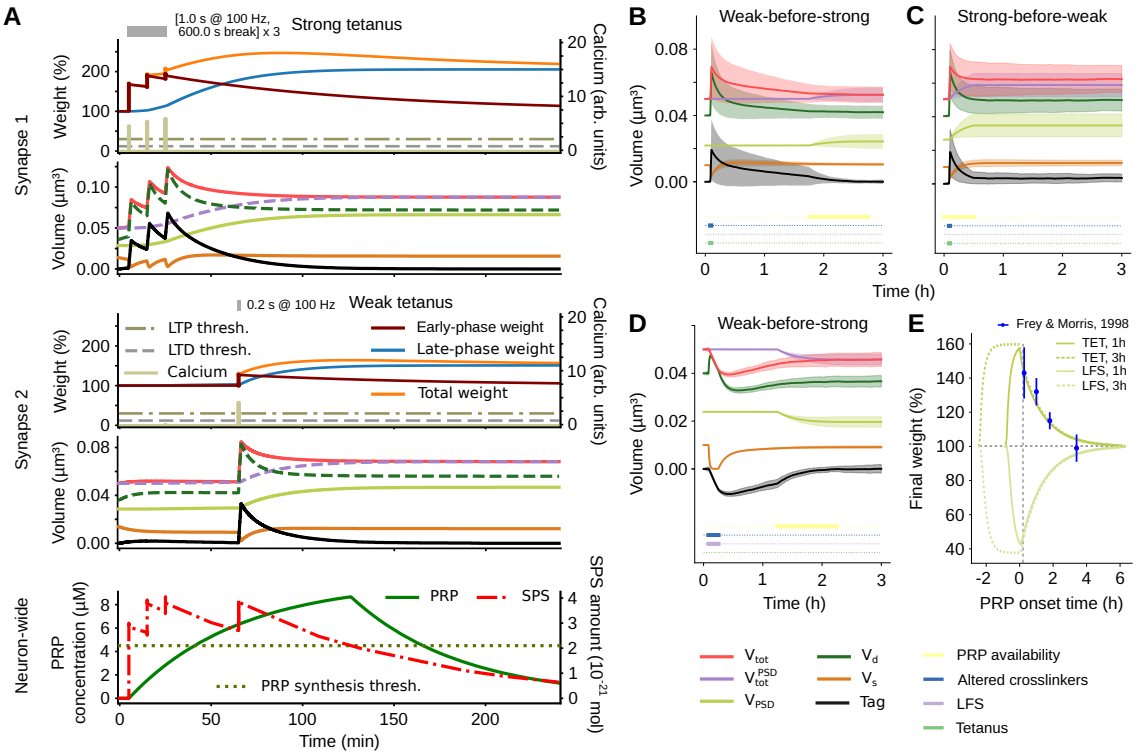

Fig. 4 Heterosynaptic plasticity via tagging-and-capture. (A) Example of a strong-before-weak tetanization protocol in the full-integrated model (strong tetanus via first synapse starting at 300 s, weak tetanus via second synapse starting at 3900 s, cf. Fig. 3); (B) weak-before-strong tetanization in the late-phase only model; (C) same for strong-before-weak tetanization; (D) same for weak-before-strong low-frequency stimulation. (E) Final values of V_{tot} and V_{PSD} in the late-phase-only model after weak tetanus (vivid color) and LFS (pale color), under systematic variation of the onset time of PRP availability due to a strong stimulus. Strongest plasticity occurs when PRP is available at the time of the weak stimulus. For PRP availability before the stimulus, the duration of PRP availability (1 h solid line, 3 h dashed line) determines the maximal time difference between strong and weak stimuli. The dashed vertical line marks the PRP availability used for the reduced model in the rest of the study. Experimental results [47] are shown for comparison (data points in blue).

Heterosynaptic plasticity via tagging-and-capture and the decay of the tag

As a next step, we investigated the behavior of our model under tagging-and-capture protocols for heterosynaptic plasticity. Specifically, we tested whether the proposed tag also shows the expected behavior if protein synthesis is triggered by stimulation at another synapse. For this, we apply weak and strong stimuli, with a time delay between them, at different synapses of the same neuron. The weak stimulus generates a synaptic tag at the stimulated synapse, but does not trigger PRP synthesis and thus no late-phase plasticity. Complementary to this, the strong stimulus at another synapse elicits PRP synthesis, such that newly synthesized PRPs can be used by the tag at the weakly stimulated synapse to form late-phase plasticity.

To test the according behavior of our fully-integrated model, we simulated a situation where the strong stimulus arrives before the weak stimulus. For this we find that the weak stimulus, which by itself could not cause changes of the late-phase weight (Fig. 3A), now indeed leads to a persistent increase in the PSD volume and, thus, the late-phase-weight (Fig. 4A, panels for synapse 2). Knowing that the full-integrated model captures this behavior, we systematically analyzed the determinants of heterosynaptic tagging-and-capture using our proof-of-concept actin-PSD model. We focused on the emergence of late-phase plasticity at the weakly stimulated synapse, considering that PRP synthesis is triggered by a strong stimulus at another synapse at a time before (strong-before-weak protocol, Fig. 4C) and after the weak plasticity event (weak-before-strong protocol, Fig. 4B, D). When the strong stimulus arrives after a weak tetanus (Fig. 4B), PRPs become available later than for the usual homosynaptic LTP (Figs. 2 and 3). At this time the total volume of the actin pools has almost decayed back to its initial value, and hence the adaptation of V_{PSD} needed to match this volume becomes smaller. Accordingly, we observe a decreased magnitude of late-phase LTP for a weak-before-strong tetanic protocol. Similarly, also for a weak LFS arriving before a strong stimulus (Fig. 4D), we observe a decreased magnitude of late-phase LTD. In contrast, for the strong-before weak protocol, PRP is available at the weakly stimulated synapse already at the time of stimulation such that the magnitude of late-phase changes is larger (Fig. 4C).

We then systematically varied the onset time of PRP availability, finding that the maximal effect of both LTP and LTD is achieved if PRP synthesis starts together with the weak stimulus (Fig. 4E). If the strong stimulus occurs before the weak one, PRPs are available upon the weak stimulation and V_{PSD} quickly adapts to balance the mismatch with the actin volumes (Fig. 4C). However, PRPs need to be available until the stimulus-induced imbalance of the actin volumes and the PSD volume at the weakly stimulated synapses are fully equilibrated. Otherwise, the PSD dynamic will stop early and the rest of the equilibration is only achieved by dynamic pool changes (slower decay after $t = 30\,\mathrm{min}$ in Fig. 4C). Hence, the duration of PRP availability determines how long before the weak stimulus the strong one can be started to yield maximal late-phase plasticity. If PRPs are available for one hour, maximal plasticity is achieved when the PRP synthesis starts immediately at the weak stimulus (Fig. 4E, solid lines). However, PRPs may be present for many hours [48], and therefore, we also tested a prolonged PRP availability of 3 hours (Fig. 4E, dashed lines). In this

case, PRP synthesis could start up to 1.5 hours before the stimulus and still lead to maximal changes. On the other hand, if PRP synthesis starts after the stimulus (weak-before-strong), we observe the same gradual decay of the late-phase plasticity for both cases. Here, initially only the dynamic pool volume adapts to the PSD and decreases the imbalance. Consequently, less change of the PSD is needed to match the volume once PRPs are available, and the overall change of the PSD is smaller (Fig. 4B and E). By assessing the decline of this overall PSD change with the temporal distance between weak and strong stimulus, one can evaluate the lifetime of the tag (Fig. 4E). For our model, we selected the parameter values such that this relationship matches the one found in electrophysiological experiments (Fig. 4E blue data points based on [47]). For low-frequency stimulation and LTD, the resulting curves are qualitatively similar, but for decreased instead of increased weights (Fig. 4D and E).

Taken together, these findings show that the proposed synaptic tag can account for the capture of PRPs triggered by stimuli at other synapses while exhibiting a realistic decay over time.

Impact of multiple subsequent stimuli at the same synapse

So far, we have only considered a single stimulus at each synapse. Yet, there may be multiple stimuli at the same synapse which jointly determine the synaptic tag and, thus, the long-term plasticity of the synapse. Hence, as a last step, we evaluate the response of our actin-PSD model to multiple plasticity-inducing stimuli. To reduce complexity, we restrain our analysis to the late-phase-only plasticity model.

First, we tested how consecutive tetanic and low-frequency stimuli would influence the weights in our model. We find that for a sufficiently small inter-stimulus interval (e.g., 5 minutes in Fig. 5A), there will be no late-phase plasticity, indicating that the tags from LTP and LTD events cancel each other out. However, for longer inter-stimulus intervals we observe that late-phase potentiation re-emerges (Fig. 5B), which is consistent with electrophysiological [49] and spine volume data [50] on tag resetting. Thus, we conclude that our model can also reproduce the late-phase plasticity produced by two subsequent, interacting stimuli as expected from tag resetting experiments.

Finally, as a prediction of our model, we tested whether the lasting late-phase changes from multiple LTP- or LTD-inducing stimuli would sum linearly and how the timing between the stimulation events would influence this. For this, we first applied two high-frequency (tetanic) stimuli separated by a defined time interval (e.g., 2 h as shown in Fig. 5C) and evaluated the PSD size after all quantities had equilibrated. We compare these with the result of a single LTP event (blue dashed line in Fig. 5D) and of two consecutive but sufficiently separated LTP events (green dashed line, Fig. 5D). We observe that, for inter-stimulus intervals of a few minutes, the resulting volume and PSD size are smaller than for two independent events (sub-linear summation), indicating an occlusion of LTP (see [51] for experimental evidence of this). After that, however, we observe a super-linear summation of the LTP events for inter-stimulus intervals of up to around 75 minutes. After this interval, the PRP availability of the first stimulus has vanished and there is no influence on the second stimulus such that the results match those of two far separated LTP-events (linear stacking).

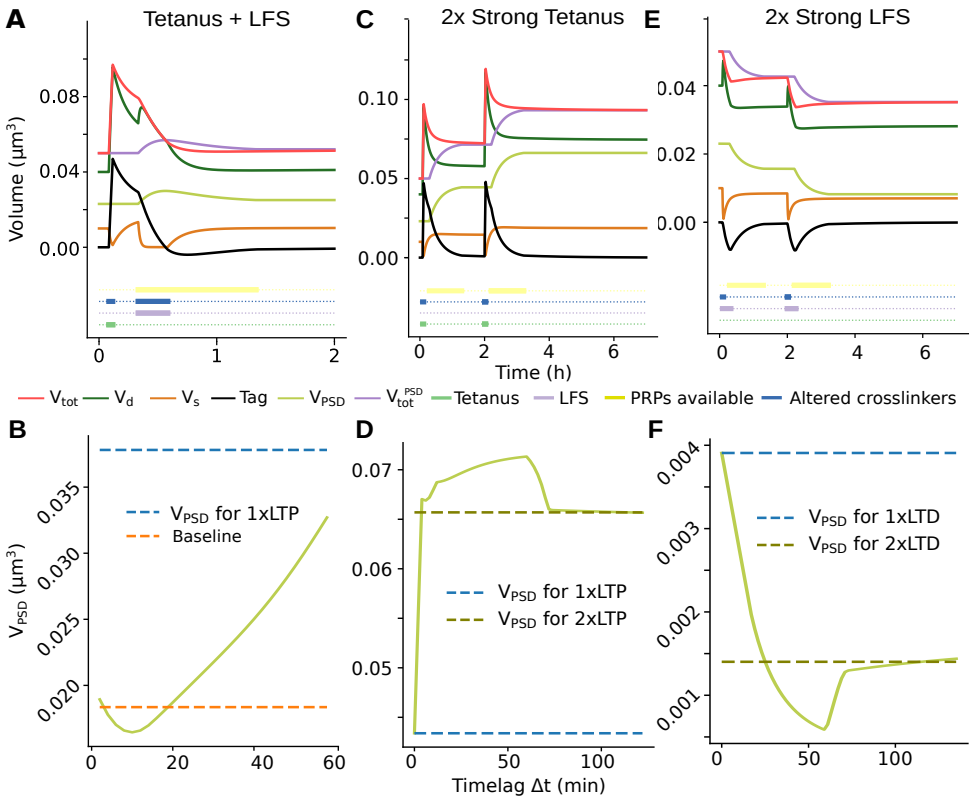

Fig. 5 Impact of two temporally separated stimuli at one synapse. (A) Tag resetting: a strong LFS 5 min after a strong tetanus stimulus blocks the late-phase LTP effect. (B) Systematic analysis of the tag resetting effect depending on the LTP-LTD temporal lag, which reveals that tag resetting only works within a short time window after tag setting. (C) The effect of two strong tetanus stimuli accumulates linearly when they are sufficiently separated (here by 2 hours). (D) Dependence of the plasticity effect (i.e., of the final value of V_{PSD}) on the temporal lag between two strong tetanus stimuli. (E) The effect of two strong LFS stimuli (again separated by 2 hours) accumulates linearly as well. (F) Dependence of the plasticity effect on the temporal lag between two strong LFS stimuli.

We further assessed how the temporal spacing between two low-frequency stimuli influences LTD (Fig. 5E and F). Similar as for LTP, we observe weaker LTD (sub-linear summation) for inter-stimulus-intervals up to around 45 minutes and stronger LTD (super-linear summation) in a time window from 45 to 75 minutes after the first stimulus (Fig. 5F).

Taken together, most importantly, our model predicts that around an hour after a first stimulus has been received, a repeated stimulus causes a stronger plasticity effect. This may relate to psychological effects such as spaced learning [52].

Discussion

To provide a mechanistic description of the synaptic tag, we have derived a biophysically interpretable reaction rate model of actin and the PSD, which are the key players

in structural and functional synaptic plasticity. Our model can reproduce experiments not only on homosynaptic late-phase LTD and LTP but also on heterosynaptic synaptic tagging-and-capture experiments. In summary, we conclude from our findings that the mismatch between the spine volume induced by actin dynamics and the volume expected from the PSD size constitutes a viable candidate implementation for the synaptic tag.

Our proof-of-concept model further provides predictions for the interaction of multiple, temporally adjacent stimuli that can be tested in experiments (cf. [51, 52]). Most established phenomenological models of synaptic plasticity do not include interaction of consecutive stimuli on a timescale of minutes (cf. [53–55]). Yet, it can be very beneficial for neural systems: On the one hand, the adaptation of synaptic weights needs energy, and it is likely that the brain would employ plasticity mechanisms that are energy-efficient [56]. Recent research has shown that this energy-efficiency can be achieved by having a fast plasticity mechanism with small energy cost that integrates over a few stimuli and a slow plasticity mechanism with larger energy cost that adapts the synaptic weights only if needed [57]. In our model the fast process would be implemented by the structural changes that induce a continuous synaptic tag which is manifested by the imbalance between actin volumes and PSD in our model. Through multiple stimuli, this imbalance can be enlarged or shrinked and even pushed to the opposite sign. This process is likely energy-efficient as it is sufficiently implemented by slight tweaks of the local actin dynamics. The slow plasticity mechanism, given by the adaptation of the PSD, then transfers the tag into actual functional changes. This can be considered to be less energy-efficient as it involves *de novo* protein synthesis and/or transport of molecules (such as proteins or mRNA) from the soma. On the other hand, two-phase plasticity mechanisms have also been proposed to enhance storage capacity in neural networks [58–61]. In contrast to earlier plasticity models that often assume bistable late-phase weights, a line attractor, as considered here, may improve storage capacity by allowing for a continuous range of synaptic weights. For example, it can facilitate the storing of overlapping ensembles of neurons [62], where simpler bistable models would suffer from interference due to their inability to integrate multiple increases in synaptic weight (also see our investigations in Fig. 5). In theory [63], the line attractor can enable networks to store memory representations with an optimized set of weights, mitigating catastrophic forgetting and improving storage capacity.

Finally, the implementation of our full-integrated model with the Arbor simulator (see Methods) allows to seamlessly deploy the model in future network simulations with single- or multi-compartment neurons (cf. [64]). In particular, our own previous network models [19, 62, 65], which have considered a simpler model of synaptic tagging-and-capture combined with the same calcium-based model of early-phase plasticity that we used here, may thus easily be extended to account for the biophysically more realistic actin-based formulation that we have presented here. This may provide more detailed insights into the impact of multiple stacked learning stimuli as mentioned above (cf. [62]), the impact of the timing of PRP synthesis at the network level (possibly depending on neuromodulators, cf. [65]), as well as the priming of memory

representations on timescales of the synaptic tag [62]. Furthermore, with few adjustments, also other network models featuring synaptic tagging-and-capture ([17, 60, 66], see [67] for a review) may be improved by adding our proposed biophysical late-phase mechanisms.

Methods

Actin-based model of tagging-and-capture

Long-lasting synaptic alterations due to synaptic tagging-and-capture are known to depend on dynamic actin [74, 75]. Changes in actin dynamics affect spine geometry, which is followed by alterations of postsynaptic density [37]. These, in turn, correlate with the number of bound AMPA receptors and, thus, the synaptic weight. Following this reasoning, we model tagging-and-capture based on the amount of dynamic, fast-treadmilling actin (via the volume V_d induced by the dynamic pool), the amount of

Param.	Value	Description	Reference
k_growth	$135 \cdot 10^{-6}\,\mathrm{s}^{-1}\ \mu\mathrm{m}^3$	growth rate of the dynamic actin pool	
k_decay	$1/380\ \mathrm{s}^{-1}$	decay rate of the dynamic actin pool	[5]
τ_PSD	380/0.255 s	adaptation rate of the PSD (with PRPs)	[37]
c_0	0.725	basal fraction of dynamic actin	
τ_c	0.0488 s	calcium timescale	[18, 19, 45]
c_pre	1	calcium increase per presynaptic spike	[18, 19, 45]
c_post	0.2758	calcium increase per presynaptic spike	[18, 19, 45]
t_cad	0.0188 s	delay of calcium increase with respect to presynaptic spike	[18, 19, 45]
θ_p	3.0	potentiation threshold	[18, 19]
θ_d	1.2	depression threshold	[18, 19]
θ_CaMKII	5.0	threshold for CaMKII activity	
γ_p	1645.6	early-phase potentiation rate	[45]
γ_d	313.1	early-phase depression rate	[45]
τ_h	688.4 s	early-phase weight timescale	[45]
σ_wn	2.90436 mV	scaling factor for fluctuations of early-phase plasticity	[45, 62]
τ_CaMKII	120 s	timescale of CaMKII deactivation	[68, 69]
τ_CaN	120 s	timescale of CaN deactivation	[69]
θ_ϕ	2.10037 mV	PRP synthesis threshold	[18]
τ_ϕ	3600 s	PRP timescale	[15, 18]
ϕ_max	10.0 µmol/l	equilibrium (maximum) concentration of PRPs under ongoing synthesis	[15, 18, 64]
f_int	0.1 l/µmol	scaling of the integration of PRPs into the PSD	[64]
c_w	4.20075 mV	constant determining the initial value and dynamics of the total synaptic weight	[45, 62]
c_late	0.8	late-phase fraction of the total weight	[18, 19]
τ_mem	10 ms	membrane time constant	[53, 70]
τ_syn	5 ms	synaptic time constant	[53, 70, 71]
t_axd	3 ms	axonal transmission delay	[70, 72]
t_ref	2 ms	absolute refractory time	[53, 73]
V^rev	−65 mV	reversal (equilibrium) voltage	[53]
V^th	−55 mV	threshold voltage for firing	[53]
V^reset	−70 mV	reset voltage	[53]

Table 1 Parameter values and sources for both the late-phase model and the other parts of the full-integrated model.

Stimulus	Birth γ	Death μ	$\langle n_\mathrm{f} \rangle$	k_b	k_u	Interval	PRPs available
Basal	0.02 s^{-1}	0.5 s^{-1}	0.04	1/2480 s^{-1}	1/620 s^{-1}	-	-
Weak tetanus	0.45 s^{-1}	0.5 s^{-1}	3.12	1/55000 s^{-1}	1/55 s^{-1}	[0 s, 60 s]	-
Strong tetanus	0.45 s^{-1}	0.5 s^{-1}	3.12	1/55000 s^{-1}	1/55 s^{-1}	[0 s, 120 s]	[900 s, 4300 s]
Weak LFS	0.0 s^{-1}	0.05 s^{-1}	0.0	1/55000 s^{-1}	1/55 s^{-1}	[0 s, 600 s]	-
Strong LFS	0.0 s^{-1}	0.05 s^{-1}	0.0	1/55000 s^{-1}	1/55 s^{-1}	[0 s, 900 s]	[900 s, 4300 s]

Table 2 Time-dependent changes of the crosslinker and actin foci dynamics after stimulation. The reported $\langle n_\mathrm{f} \rangle$ is used in simulations, where the birth-death-process is replaced by a constant n_f-value and tuned to yield results comparable to the stochastic simulations.

cross-linked, stable actin (via the volume V_s induced by the stable pool), and the size of the postsynaptic density (via the volume V_PSD induced by the postsynaptic density). The dynamics of the system are given by:

$$\begin{aligned} \frac{dV_\mathrm{d}}{dt} &= -k_\mathrm{b}(t)V_\mathrm{d} + k_\mathrm{u}(t)V_\mathrm{s} + k_\mathrm{growth} n_\mathrm{f}(t), \\ &\quad -k_\mathrm{decay}\left[\frac{V_\mathrm{d}}{V_\mathrm{d}+V_\mathrm{s}} - c_0\right]_+ \left[V_\mathrm{d} + V_\mathrm{s} - V_\mathrm{PSD}\right]_+ , \qquad (1) \\ \frac{dV_\mathrm{s}}{dt} &= +k_\mathrm{b}(t)V_\mathrm{d} - k_\mathrm{u}(t)V_\mathrm{s}, \qquad (2) \\ \frac{dV_\mathrm{PSD}}{dt} &= \phi(t)\cdot\left(V_\mathrm{d} + V_\mathrm{s} - V_\mathrm{tot}^\mathrm{PSD}\right)/\tau_\mathrm{PSD}. \qquad (3) \end{aligned}$$

Here, k_b and k_u are the crosslinker binding and unbinding rates, k_growth and k_decay the rates for dynamic pool growth and shrinkage, $\phi(t)$ the PRP availability, τ_PSD the PSD reorganization timescale, $[x]_+ = (x + |x|)/2$ the rectification function, and n_f the number of active polymerization foci. More detailed simulations of the actin network suggest that n_f fluctuates heavily because new foci continuously emerge while old foci die out [22, 25]. To approximate this, we here determine n_f by a birth-death process, with a birth rate γ and a death rate μ.

While

$$V_\mathrm{tot} = V_\mathrm{d} + V_\mathrm{s}$$

represents the total volume of the spine determined by the actin dynamics,

$$V_\mathrm{tot}^\mathrm{PSD} = V_\mathrm{PSD} + V_n^* \text{ with } V_n^* = \frac{k_\mathrm{growth}\cdot\langle n_\mathrm{f}\rangle}{k_\mathrm{decay}}\left(\frac{k_\mathrm{u}}{k_\mathrm{b}+k_\mathrm{u}} - c_0\right)^{-1}$$

is the steady-state volume that can be expected for the current PSD size with dynamic actin in its basal state (which induced the correction V_n*; see Appendix). Here, $\langle . \rangle$ denotes the temporal average (in basal state). Note, in the absence of dynamic actin foci ($n_\mathrm{f} = 0$), $V_\mathrm{tot}^\mathrm{PSD}$ equals V_PSD.

Time-dependent parameters during LTP and LTD induction

During plasticity, the crosslinker binding and unbinding as well as the birth and death rate of actin foci are altered as described in the following. All constant parameters are reported in Table 1.

After stimulation, the actin cytoskeleton can undergo highly dynamic changes as actin-binding proteins change their concentrations and binding rates. For example, cofilin gets activated after an LTP-inducing stimulus, which leads to a massive severing and, in turn, produces an abundance of free actin and creates new foci [27, 30]. Moreover, crosslinkers unbind from the filaments [26, 27, 30]. Although not so well documented, the latter may also occur for LTD [42, 43].

In order to study our actin-PSD model (Eqs. 1–3) during plasticity, we first implemented time-dependent parameters in the form of step functions, which switch their value at given time-points after a putative LTP or LTD event. We used the following alterations, which are summarized in Table 2:

Weak and strong stimulations

In general, strong stimuli induce late-phase plasticity, while weak stimuli only induce early-phase effects. Thus, for weak stimuli, the duration of the rate alterations is smaller and $\phi(t)$ is kept at zero throughout the experiment. In contrast, for strong stimuli, we set the PRP availability to $\phi \equiv 1$ for 60 minutes starting 15 minutes after the stimulus (if not stated otherwise; also cf. PSD changes in [37]).

Tetanic stimulation

Tetanic, i.e., high-frequency stimulation can induce LTP. Accordingly, immediately after a tetanic stimulation event, the birth rate of the stochastic process is significantly increased for the typical duration of a tetanization protocol (60 s/120 s for weak and strong, respectively). This corresponds to an increase of cofilin in the spine, which has experimentally been observed in the early phase of LTP [30]. Also, within the first minutes of LTP, crosslinkers unbind from actin and/or leave the spine [30, 42, 76]. Therefore, in the model, the crosslinker binding and unbinding rates k_b and k_u rates are increased to allow faster exchange between the two pools, shifting their balance towards unbinding, which results in a smaller stable actin pool.

Low-frequency stimulation (LFS)

LFS can give rise to LTD. Accordingly, in our model, we set the birth rate of actin foci to zero and adapt the death rate for the duration of the stimulus (600 s/900 s). The crosslinker binding rates are subject to the same transformation as in LTP, but in this case, the duration of the effect is prolonged to remain for the duration of the LTD stimulus.

Parameter estimation based on experimental data

To find parameters that match experimental characterizations of synapses, we used three different datasets: (1) volume time courses after glutamate uncaging inducing LTP [40] and (2) LTD [41], as well as (3) electrophysiological data from the weak-before-strong protocol [47]. For each datapoint, we calculated the squared error of the relative volume changes, normalized by the size of the experimentally observed volume change. We weighted the errors of the 3 datasets with $w = (1, 2, 10)^T$ to account for the imbalance between the number of data points, and calculated the sum over all these

weighted normalized errors. We then minimized this error. For numerical stability, we used the inverse of the rates as well as the product of covariant parameters as free parameters (with their bounds in brackets):

- the timescale for crosslinker unbinding $1/k_{\mathrm{u}} \in [300\,\mathrm{s}, 1500\,\mathrm{s}]$
- the dynamic pool decay timescale $1/k_{\mathrm{decay}} = 240\,\mathrm{s}$ (varied in step 2 only, see below)
- the ratio between dynamic pool decay and PSD adaptation timescales $\in [0.05, 0.5]$
- the product (mean) number of active foci and the growth rate k_{growth}, $\in [4 \cdot 10^{-5} \cdot V_{\mathrm{tot}}^{\mathrm{PSD}}(t=0),\, 2 \cdot 10^{-4} \cdot V_{\mathrm{tot}}^{*}(t=0)]$
- same product during LTP $\in [6 \cdot 10^{-3} \cdot V_{\mathrm{tot}}^{\mathrm{PSD}}(t=0),\, 2 \cdot 10^{-2} \cdot V_{\mathrm{tot}}^{\mathrm{PSD}}(t=0)]$
- the offset fraction of the dynamic pool $c_0 \in [0.7, 0.75]$

For minimization, we used a two-step procedure:

1) Bayesian optimization: Using the Bayesian Optimization package [77], we scanned for local optima in the above specified parameter regime by using 200 initial samples and 50 samples from the Optimizer.
2) Minimizer The resulting best parameter set was then passed to a gradient descent optimizer (Nelder-Mead from scipy optimize) in order to reach the local minimum. Here, the parameter changes were bounded within 10% of the initial value. Throughout the process, rates were rounded to multiples of 5 s.

After that, the ratio between binding and unbinding timescales was set to 1/4 to obtain 20% stable pool fraction [28].

Fully integrated model with calcium-based early-phase plasticity and PRP synthesis

In order to study its interaction within neurons and neural circuits, we coupled our model of late-phase plasticity to established models for neuronal activity, calcium-based early-phase plasticity, and PRP synthesis (cf. [18, 19, 67]). Large parts of the formulation below thus follow previous descriptions [19, 62]. Note that as compared to [19, 62], we use here a transformed formulation of the early- and late-phase dynamics where the baseline of the early-phase weights is $h(t=0) = 0$ and the baseline of the late-phase weights is $z(t=0) = c_w$. This formulation is equivalent to the one in the previous studies, but may be easier to interpret from a biological perspective (the baseline of the total weight is here set by the stable late-phase weight).

Calcium

LTP and LTD are known to rely on calcium signaling both on a morphological and functional level [40, 45, 46]. Therefore, in our model, the calcium level $c_{ji}(t)$ at the postsynaptic site of a synapse from neuron i to neuron j is the major factor to induce plasticity. Following [45], the calcium level is increased by c_{pre} for every presynaptic spike at time t^n and by c_{post} for every postsynaptic spike at time t^m, and it evolves according to:

$$\frac{dc_{ji}(t)}{dt} = -\frac{c_{ji}(t)}{\tau_c} + c_{\text{pre}} \sum_{t' \in S(i)} \delta(t - t' - t_{\text{cad}}) + c_{\text{post}} \sum_{t' \in S(j)} \delta(t - t'), \tag{4}$$

where $S(i)$ and $S(j)$ mark the set of spike times of neurons i and j, respectively, $\delta(\cdot)$ is the Dirac delta distribution, τ_c is a time constant, and t_{cad} accounts for the delayed increase of calcium for presynaptic spikes.

Early-phase plasticity

Early phase-plasticity is based on altered receptor trafficking driven by the calcium concentration in the postsynaptic spine [35, 78]. We model this by an early-phase weight $h(t)$ following a calcium-based plasticity rule with two thresholds for depression and potentiation, respectively [18, 19, 45]. The dynamics are described by:

$$\begin{aligned}\tau_h \frac{dh_{ji}(t)}{dt} = &-0.1 \cdot h_{ji}(t) + \gamma_{\text{p}} \cdot (10\,\text{mV} - (h_{ji}(t) + c_w)) \cdot \Theta(c_{ji}(t) - \theta_{\text{p}}) \\ &-\gamma_{\text{d}} \cdot (h_{ji}(t) + c_w) \cdot \Theta(c_{ji}(t) - \theta_{\text{d}}) + \xi(t),\end{aligned} \tag{5}$$

where $\Theta(\cdot)$ is the Heaviside step function, c_w is a constant that determines the initial value and dynamics of the total synaptic weight, τ_h is the calcium decay time constant, $c_{ji}(t)$ is the calcium concentration at the postsynaptic site, and $\xi(t)$ is a noise term (see below).

The first term on the right-hand side describes the relaxation of the early-phase weight to zero, the second term describes the induction of early-phase LTP with rate γ_{p} (requiring that the calcium amount is above the threshold θ_{p}), and the third term describes the induction of early-phase LTD with rate γ_{d} (requiring that the calcium amount is above the threshold θ_{d}). As the latter two terms are multiplied by $(h_{ji}(t) + c_w)$ and $(10\,\text{mV} - (h_{ji}(t) + c_w))$, the early weight is soft-bounded to an interval $[-c_w, 10\,\text{mV} - c_w]$. Finally, the noise term depends on Gaussian white noise $\Gamma(t)$ with mean zero and variance $1/dt$, and is given by (cf. [45])

$$\xi(t) = \sqrt{\Theta\left(c_{ji}(t) - \theta_{\text{p}}\right) + \Theta\left(c_{ji}(t) - \theta_{\text{d}}\right)} \cdot \sqrt{\tau_h} \cdot \sigma_{\text{wn}} \cdot \Gamma(t),$$

with the factor σ_{wn} scaling its standard deviation.

Synthesis of PRPs

Synthesis of plasticity-related products (PRPs), in particular, of proteins, has been found to occur in the soma as well as locally in dendrites. In our full-integrated model, we describe PRP dynamics as a process of synthesis and decay that may occur neuron-wide or in a locally clustered manner. To determine the onset of PRP synthesis, we define a "signal triggering PRP synthesis" (SPS) as the absolute deviation of the early-phase weights from their stationary value 0 summed over all considered incoming

synapses (cf. [18]):

$$\mathrm{SPS}_j(t) = \sum_j |h_{ji}(t)|$$

If this is larger than a threshold θ_ϕ, then the amount of PRP $\phi_j(t)$ increases to a maximum value $\phi_{\max}$, whereas it decays to the baseline zero otherwise:

$$\tau_\phi \frac{d\phi_j(t)}{dt} = -\phi_j(t) + \phi_{\max} \cdot \Theta(\mathrm{SPS}_j(t) - \theta_\phi) \tag{6}$$

Here, the timescale of the dynamics is given by the constant τ_ϕ.

Coupling of early-phase dynamics to the actin-PSD model of late-phase plasticity

The changes in the dynamics of actin-binding proteins during LTP and LTD are induced by calcium-dependent signaling cascades [27]. In particular, the signaling chain depending on calcineurin (CaN) is activated by intermediate calcium levels during LTD, whereas the signaling chain downstream of CaMKII is typically activated by very high calcium levels and triggers LTP in further downstream signaling. Following this, in our integrated model, CaMKII and CaN are set to CaMKII $\equiv 1.0$ and CaN $\equiv 1.0$ whenever the calcium concentration fulfills $c(t) > \theta_{\mathrm{CaMKII}}$ and/or $c(t) > \theta_{\mathrm{d}}$, respectively (cf. Eq. 4).

Otherwise, the concentrations of CaMKII and CaN decay exponentially following

$$\frac{d\mathrm{CaMKII}_{ji}}{dt} = -\mathrm{CaMKII}_{ji}/\tau_{\mathrm{CaMKII}}, \qquad \frac{d\mathrm{CaN}_{ji}}{dt} = -\mathrm{CaN}_{ji}/\tau_{\mathrm{CaN}}. \tag{7}$$

Altered dynamics for the crosslinkers and the birth-death process are applied if one or both of the signals are above a threshold of 0.5. For simplicity, we do not explicitly simulate the birth-death process for actin foci in the full-integrated model, but instead use the expected mean values for n_{f} as given in Table 2. Thus, k_{b}, k_{u} and n_{f} for each synapse are set to the values for potentiation from Table 2 when CaMKII-signaling is on ($\mathrm{CaMKII}_{ji} > 0.5$), to the values for depression when only CaN-signaling is on ($\mathrm{CaMKII}_{ji} < 0.5$ and $\mathrm{CaN}_{ji} > 0.5$), and to the basal values otherwise.

Finally, in our integrated model, we use the PSD-dependent volume V_{PSD} as a proxy for the late-phase weight z (cf. [19, 62]) in the following way:

$$z(t) = c_w + \left(\frac{V_{\mathrm{PSD}}(t)}{V_{\mathrm{PSD}}(0)} - 1 \right) \cdot c_w \cdot c_{\mathrm{late}}, \tag{8}$$

where c_w is a constant determining the unscaled initial weight and the weight dynamics, and c_{late} determines the ratio by which the late-phase weight enters the total weight. The late-phase weight is then added to the early-phase weight h to yield the total weight of the synapse:

$$w(t) = h(t) + z(t). \tag{9}$$

Note that as mentioned above, this is a transformed formulation as compared to [19, 62].

Neuronal dynamics and connectivity

To model the neuronal membrane dynamics, we employed the leaky integrate-and-fire formalism, given by

$$\tau_{\mathrm{mem}} \frac{dV_j(t)}{dt} = V^{\mathrm{rev}} - V_j(t) + V_j^{\mathrm{PSP}}(t) + V_j^{\mathrm{stim}}(t), \tag{10}$$

for the neuron with index j. Here, V^{rev} is the reversal potential, τ_{mem} is the membrane time constant, $V_j^{\mathrm{PSP}}(t)$ is the sum of postsynaptic potentials, and $V_j^{\mathrm{stim}}(t)$ accounts for the external stimulation (see the following subsection). With the synaptic weights w_{ji} (see Eq. 9) and the set $S(i)$ of the presynaptic spike times, the postsynaptic potential is given by:

$$V_j^{\mathrm{PSP}}(t) = \sum_i \sum_{t' \in S(i)} w_{ji} \cdot \exp\left(-\frac{t - t' - t_{\mathrm{axd}}}{\tau_{\mathrm{syn}}}\right) \cdot \Theta(t - t' - t_{\mathrm{axd}}), \tag{11}$$

where t_{axd} is the axonal delay time, τ_{syn} is the synaptic time constant, and $\Theta(\cdot)$ is the Heaviside step function. A spike is triggered if the neuronal membrane voltage $V_j(t)$ crosses the threshold V^{th}, following which the membrane voltage is set to V^{reset}, where it remains for the refractory time t_{ref} (see Table 1 for the parameter values).

For the single-synapse paradigms shown in Fig. 3, we used two such neurons, connected by one synapse described by our integrated model of early- and late-phase synaptic plasticity with the calcium traces driven by the pre- and postsynaptic neuronal spikes. The presynaptic neuron was subject to the stimulation protocols described in the following subsection.

For the strong-before-weak paradigm in Fig. 4, we used three neurons $\{0, 1, 2\}$ with the connections $1 \to 0$ and $2 \to 0$. In this context, neuron 1 received strong stimulation and neuron 2 received weak stimulation, as detailed in the next subsection.

Note that our freely provided Arbor program code can be used to explore the dynamics of our plasticity model in a wide variety of paradigms, including large-scale neural circuits.

Stimulation protocols

To induce l-LTP, l-LTD, e-LTP only, and e-LTD only, we chose classical well-established stimulation protocols (cf. [18, 19, 39]). As described in the previous subsection, we conveyed these protocols by forcing a presynaptic neuron to spike with Poisson-distributed spike times, which can be used to model the firing of a neuron at a certain average rate (cf. [53]). The details of the protocols are described in the following.

Strong tetanic stimulation (STET). This protocol serves to induce l-LTP. It consists of three pulses of 100 Hz stimulation, each lasting for 1.00 s. The pulses are separated by breaks of 600 s.

Weak tetanic stimulation (WTET). This protocol serves to induce e-LTP. It consists of one pulse of 100 Hz stimulation, lasting for 0.20 s.

Strong low-frequency stimulation (SLFS). This protocol serves to induce l-LTD. It consists of 900 pulses of 20 Hz stimulation, each lasting for 0.15 s. The pulses are separated by breaks of 1.00 s.

Weak low-frequency stimulation (WLFS). This protocol serves to induce e-LTD. It consists of one long period of 1 Hz stimulation, lasting for 900 s.

Software

For the late-phase-only model, we used a custom Python implementation that was designed to enable easy switching between simulation paradigms.

The full-integrated model was implemented using the Arbor simulator library [64, 79], which is particularly well suited for the efficient execution of network simulations with multi-compartment neurons on high-performance computing hardware, and will thus allow for future network simulations employing our model.

We will make our simulation code freely available upon publication of this article.

Supplementary information. **Appendix A:** Fixed-point and stability analysis for the late-phase model

Declarations

Funding. This work was supported by the German Research Foundation (Deutsche Forschungsgemeinschaft, DFG) through grants SFB1286 (projects C01, C03 and Z01).

Conflict of interest. There is no conflict of interest

Code availability. Code will be made available in public repositories upon publication

Author contribution. Conceptualization: FN, JL, CT, MF; Formal Analysis: FN, JL, MF; Funding acquisition: MF, CT; Investigation: FN, JL, MF; Methodology: FN, JL, CT, MF; Project administration: CT, MF; Software: FN, JL; Supervision: CT, MF; Visualization: FN, JL, MF; Writing – original draft: JL, MF; Writing – review & editing: FN, JL, CT, MF.

Appendix A: Fixed-point and stability analysis for the late-phase model

Here, we want to calculate the fixed points of our model under constant parameter values and analyze their stability. For this we first replace the stochastic birth-death-process that determines the number of foci with the current expected value, corresponding to the temporal mean $\langle n_\mathrm{f} \rangle$, to arrive at a non-stochastic dynamic system. We further simplify the calculation by defining $V_\mathrm{tot} = V_\mathrm{d} + V_\mathrm{s}$ and only investigating the dynamic of a two-dimensional system. When the crosslinker binding and unbinding are in equilibrium, the dynamic and stable pool can be obtained as fractions of V_tot:

$$V_\mathrm{d}^* = \frac{k_\mathrm{u}}{k_\mathrm{b} + k_\mathrm{u}} V_\mathrm{tot}, \tag{1}$$

$$V_\mathrm{s}^* = \frac{k_\mathrm{b}}{k_\mathrm{b} + k_\mathrm{u}} V_\mathrm{tot}. \tag{2}$$

We arrive at

$$\frac{dV_\mathrm{tot}}{dt} = k_\mathrm{growth} \langle n_\mathrm{f} \rangle - k_\mathrm{decay} \left[\frac{k_\mathrm{b}}{k_\mathrm{b} + k_\mathrm{u}} - c_0 \right]_+ \left[V_\mathrm{tot} - V_\mathrm{PSD} \right]_+ .$$

Assuming that both rectifications are in their linear regime, we obtain a fixed-point for V_tot that can be expressed as function of V_PSD:

$$V_\mathrm{tot}^* = \underbrace{V_\mathrm{PSD}^* + \frac{k_\mathrm{growth} \cdot \langle n_\mathrm{f} \rangle}{k_\mathrm{decay}} \left(\frac{k_\mathrm{u}}{k_\mathrm{b} + k_\mathrm{u}} - c_0 \right)^{-1}}_{V_\mathrm{tot}^\mathrm{PSD}} . \tag{3}$$

This constitutes a continuous line of fixed points in the V_tot-V_PSD-space. In order to compute the stability of these fixed points, we first compute the Jacobian matrix of our equations evaluated at the fixed point:

$$J = \begin{pmatrix} -k_\mathrm{decay} \left(\frac{k_\mathrm{u}}{k_\mathrm{b}+k_\mathrm{u}} - c_0 \right) & k_\mathrm{decay} \left(\frac{k_\mathrm{u}}{k_\mathrm{b}+k_\mathrm{u}} - c_0 \right) \\ \frac{1}{\tau_\mathrm{PSD}} & -\frac{1}{\tau_\mathrm{PSD}} \end{pmatrix} .$$

The resulting eigenvalues are $\lambda_1 = 0$ and $\lambda_2 = -k_\mathrm{decay} \left(\frac{k_\mathrm{u}}{k_\mathrm{b}+k_\mathrm{u}} - c_0 \right) - \frac{1}{\tau_\mathrm{PSD}}$. The eigenvector for λ_1 is proportional to $(1,1)^T$ and thus aligns with the line of fixed-points. This proves that the fixed-point manifold defined by equation 3 forms a stable line attractor.

References

[1] Martin, S.J., Grimwood, P.D., Morris, R.G.: Synaptic plasticity and memory: an evaluation of the hypothesis. Annual review of neuroscience **23**(1), 649–711 (2000)

[2] Bliss, T.V., Lømo, T.: Long-lasting potentiation of synaptic transmission in the dentate area of the anaesthetized rabbit following stimulation of the perforant path. The Journal of physiology **232**(2), 331–356 (1973)

[3] Dudek, S.M., Bear, M.F.: Homosynaptic long-term depression in area ca1 of hippocampus and effects of n-methyl-d-aspartate receptor blockade. Proceedings of the National Academy of Sciences **89**(10), 4363–4367 (1992)

[4] Abraham, W.C.: How long will long-term potentiation last? Philosophical Transactions of the Royal Society of London. Series B: Biological Sciences **358**(1432), 735–744 (2003)

[5] Frey, U., Morris, R.G.: Synaptic tagging and long-term potentiation. Nature **385**(6616), 533–536 (1997)

[6] Redondo, R.L., Morris, R.G.M.: Making memories last: the synaptic tagging and capture hypothesis. Nature Reviews Neuroscience **12**, 17–30 (2011)

[7] Staubli, U., Lynch, G.: Stable depression of potentiated synaptic responses in the hippocampus with 1–5 hz stimulation. Brain Research **513**(1), 113–118 (1990) https://doi.org/10.1016/0006-8993(90)91096-Y

[8] Barrionuevo, G., Schottler, F., Lynch, G.: The effects of repetitive low frequency stimulation on control and "potentiated" synaptic responses in the hippocampus. Life sciences **27**(24), 2385–2391 (1980)

[9] Chen, Y.-L., Huang, C.-C., Hsu, K.-S.: Time-dependent reversal of long-term potentiation by low-frequency stimulation at the hippocampal mossy fiber–CA3 synapses. Journal of Neuroscience **21**(11), 3705–3714 (2001)

[10] Huang, C.-C., Liang, Y.-C., Hsu, K.-S.: Characterization of the mechanism underlying the reversal of long term potentiation by low frequency stimulation at hippocampal ca1 synapses. Journal of Biological Chemistry **276**(51), 48108–48117 (2001) https://doi.org/10.1074/jbc.M106388200

[11] Smolen, P., Baxter, D.A., Byrne, J.H.: Molecular constraints on synaptic tagging and maintenance of long-term potentiation: a predictive model. PLoS Computational Biology **8**(8), 1002620 (2012)

[12] Fonkeu, Y., Kraynyukova, N., Hafner, A.-S., Kochen, L., Sartori, F., Schuman, E.M., Tchumatchenko, T.: How mRNA localization and protein synthesis sites

influence dendritic protein distribution and dynamics. Neuron **103**(6), 1109–1122 (2019)

[13] Sun, C., Nold, A., Fusco, C.M., Rangaraju, V., Tchumatchenko, T., Heilemann, M., Schuman, E.M.: The prevalence and specificity of local protein synthesis during neuronal synaptic plasticity. Science Advances **7**(38), 0790 (2021)

[14] Martin, K.C., Kosik, K.S.: Synaptic tagging—who's it? Nature Reviews Neuroscience **3**(10), 813–820 (2002)

[15] Clopath, C., Ziegler, L., Vasilaki, E., Büsing, L., Gerstner, W.: Tag-trigger-consolidation: A model of early and late long-term-potentiation and depression. PLOS Computational Biology **4**(12), 1–14 (2008) https://doi.org/10.1371/journal.pcbi.1000248

[16] Barrett, A.B., Billings, G.O., Morris, R.G.M., Rossum, M.C.W.: State based model of long-term potentiation and synaptic tagging and capture. PLOS Computational Biology **5**(1), 1–12 (2009) https://doi.org/10.1371/journal.pcbi.1000259

[17] Ziegler, L., Zenke, F., Kastner, D.B., Gerstner, W.: Synaptic consolidation: from synapses to behavioral modeling. Journal of Neuroscience **35**(3), 1319–1334 (2015)

[18] Li, Y., Kulvicius, T., Tetzlaff, C.: Induction and consolidation of calcium-based homo-and heterosynaptic potentiation and depression. PLOS ONE **11**(8), 0161679 (2016)

[19] Luboeinski, J., Tetzlaff, C.: Memory consolidation and improvement by synaptic tagging and capture in recurrent neural networks. Communications Biology **4**(275) (2021) https://doi.org/10.1038/s42003-021-01778-y

[20] Ding, Y., Wang, Y., Cao, L.: A simplified plasticity model based on synaptic tagging and capture theory: Simplified stc. Frontiers in Computational Neuroscience **15** (2022) https://doi.org/10.3389/fncom.2021.798418

[21] Thomas, M., Bogaciu, C.-A., Rizzoli, S.O., Fauth, M.: Long-term potentiation-induced changes in actin dynamics and spine geometry persist on the timescale of the synaptic tag. Communications Biology **8**(1), 1065 (2025)

[22] Bonilla-Quintana, M., Wörgötter, F., Tetzlaff, C., Fauth, M.: Modeling the shape of synaptic spines by their actin dynamics. Frontiers in synaptic neuroscience **12**, 9 (2020)

[23] Mogilner, A., Oster, G.: Cell motility driven by actin polymerization. Biophysical journal **71**(6), 3030–3045 (1996)

[24] Fischer, M., Kaech, S., Knutti, D., Matus, A.: Rapid actin-based plasticity in

dendritic spines. Neuron **20**(5), 847–854 (1998)

[25] Bonilla-Quintana, M., Wörgötter, F., D'Este, E., Tetzlaff, C., Fauth, M.: Reproducing asymmetrical spine shape fluctuations in a model of actin dynamics predicts self-organized criticality. Scientific reports **11**(1), 4012 (2021)

[26] Okamoto, K.-I., Narayanan, R., Lee, S.H., Murata, K., Hayashi, Y.: The role of camkii as an f-actin-bundling protein crucial for maintenance of dendritic spine structure. Proceedings of the National Academy of Sciences **104**(15), 6418–6423 (2007) https://doi.org/10.1073/pnas.0701656104 https://www.pnas.org/content/104/15/6418.full.pdf

[27] Borovac, J., Bosch, M., Okamoto, K.: Regulation of actin dynamics during structural plasticity of dendritic spines: Signaling messengers and actin-binding proteins. Molecular and Cellular Neuroscience **91**, 122–130 (2018)

[28] Honkura, N., Matsuzaki, M., Noguchi, J., Ellis-Davies, G.C., Kasai, H.: The subspine organization of actin fibers regulates the structure and plasticity of dendritic spines. Neuron **57**(5), 719–729 (2008)

[29] Frost, N.A., Shroff, H., Kong, H., Betzig, E., Blanpied, T.A.: Single-molecule discrimination of discrete perisynaptic and distributed sites of actin filament assembly within dendritic spines. Neuron **67**(1), 86–99 (2010)

[30] Bosch, M., Castro, J., Saneyoshi, T., Matsuno, H., Sur, M., Hayashi, Y.: Structural and molecular remodeling of dendritic spine substructures during long-term potentiation. Neuron **82**(2), 444–459 (2014)

[31] Bonilla-Quintana, M., Wörgötter, F.: Exploring new roles for actin upon LTP induction in dendritic spines. Scientific Reports **11**(1), 7072 (2021)

[32] Quintana, M.B., Rangamani, P.: Mechanical forces promote actin-mediated structural plasticity. Biophysical Journal **122**(3), 418 (2023)

[33] Pinho, J., Marcut, C., Fonseca, R.: Actin remodeling, the synaptic tag and the maintenance of synaptic plasticity. IUBMB life **72**(4), 577–589 (2020)

[34] Holler, S., Köstinger, G., Martin, K.A., Schuhknecht, G.F., Stratford, K.J.: Structure and function of a neocortical synapse. Nature **591**(7848), 111–116 (2021)

[35] Becker, M.F.P., Tetzlaff, C.: The biophysical basis underlying the maintenance of early phase long-term potentiation. PLOS Computational Biology **17**(3), 1008813 (2021)

[36] Matsuzaki, M., Ellis-Davies, G.C., Nemoto, T., Miyashita, Y., Iino, M., Kasai, H.: Dendritic spine geometry is critical for ampa receptor expression in hippocampal

CA1 pyramidal neurons. Nature neuroscience **4**(11), 1086–1092 (2001)

[37] Meyer, D., Bonhoeffer, T., Scheuss, V.: Balance and stability of synaptic structures during synaptic plasticity. Neuron **82**(2), 430–443 (2014)

[38] Clavet-Fournier, V., Lee, C., Wegner, W., Brose, N., Rhee, J., Willig, K.I.: Pre- and postsynaptic nanostructures increase in size and complexity after LTP induction. bioRxiv (2023) https://doi.org/10.1101/2023.02.09.527812

[39] Sajikumar, S., Navakkode, S., Sacktor, T.C., Frey, J.U.: Synaptic tagging and cross-tagging: the role of protein kinase Mζ in maintaining long-term potentiation but not long-term depression. Journal of Neuroscience **25**(24), 5750–5756 (2005)

[40] Matsuzaki, M., Honkura, N., Ellis-Davies, G.C., Kasai, H.: Structural basis of long-term potentiation in single dendritic spines. Nature **429**(6993), 761–766 (2004)

[41] Noguchi, J., Hayama, T., Watanabe, S., Ucar, H., Yagishita, S., Takahashi, N., Kasai, H.: State-dependent diffusion of actin-depolymerizing factor/cofilin underlies the enlargement and shrinkage of dendritic spines. Scientific reports **6**, 32897 (2016) https://doi.org/10.1038/srep32897

[42] Sekino, Y., Koganezawa, N., Mizui, T., Shirao, T.: Role of drebrin in synaptic plasticity. Drebrin: From Structure and Function to Physiological and Pathological Roles, 183–201 (2017)

[43] Yasuda, H., Kojima, N., Hanamura, K., Yamazaki, H., Sakimura, K., Shirao, T.: Drebrin isoforms critically regulate NMDAR-and mGluR-dependent LTD induction. Frontiers in Cellular Neuroscience **12**, 330 (2018)

[44] Kasai, H., Ziv, N.E., Okazaki, H., Yagishita, S., Toyoizumi, T.: Spine dynamics in the brain, mental disorders and artificial neural networks. Nature Reviews Neuroscience **22**(7), 407–422 (2021)

[45] Graupner, M., Brunel, N.: Calcium-based plasticity model explains sensitivity of synaptic changes to spike pattern, rate, and dendritic location. Proceedings of the National Academy of Sciences **109**(10), 3991–3996 (2012)

[46] Zhou, Q., Homma, K.J., Poo, M.-m.: Shrinkage of dendritic spines associated with long-term depression of hippocampal synapses. Neuron **44**(5), 749–757 (2004) https://doi.org/10.1016/j.neuron.2004.11.011

[47] Frey, U., Morris, R.G.: Synaptic tagging: implications for late maintenance of hippocampal long-term potentiation. Trends in neurosciences **21**(5), 181–188 (1998)

[48] Chong, Y.S., Ang, S.R., Sajikumar, S.: Beyond boundaries: extended temporal

flexibility in synaptic tagging and capture. Communications Biology **8**(1), 553 (2025)

[49] Sajikumar, S., Frey, J.U.: Resetting of 'synaptic tags' is time-and activity-dependent in rat hippocampal CA1 in vitro. Neuroscience **129**(2), 503–507 (2004)

[50] Yang, Y., Wang, X.-b., Frerking, M., Zhou, Q.: Spine expansion and stabilization associated with long-term potentiation. Journal of Neuroscience **28**(22), 5740–5751 (2008)

[51] Kramár, E.A., Babayan, A.H., Gavin, C.F., Cox, C.D., Jafari, M., Gall, C.M., Rumbaugh, G., Lynch, G.: Synaptic evidence for the efficacy of spaced learning. Proceedings of the National Academy of Sciences **109**(13), 5121–5126 (2012)

[52] Smolen, P., Zhang, Y., Byrne, J.H.: The right time to learn: mechanisms and optimization of spaced learning. Nature Reviews Neuroscience **17**(2), 77 (2016)

[53] Dayan, P., Abbott, L.F.: Theoretical Neuroscience, 1st edn. The MIT Press, Cambridge/MA, USA (2001)

[54] Morrison, A., Diesmann, M., Gerstner, W.: Phenomenological models of synaptic plasticity based on spike timing. Biological Cybernetics **98**(6), 459–478 (2008)

[55] Mäki-Marttunen, T., Iannella, N., Edwards, A.G., Einevoll, G.T., Blackwell, K.T.: A unified computational model for cortical post-synaptic plasticity. Elife **9**, 55714 (2020)

[56] Pache, A., Rossum, M.C.: Energetically efficient learning in neuronal networks. Current opinion in neurobiology **83**, 102779 (2023)

[57] Li, H.L., Van Rossum, M.C.: Energy efficient synaptic plasticity. Elife **9**, 50804 (2020)

[58] Gardner-Medwin, A.R.: Doubly modifiable synapses: a model of short and long term auto-associative memory. Proceedings of the Royal Society B **238**(1291), 137–154 (1989)

[59] Fusi, S., Drew, P.J., Abbott, L.F.: Cascade models of synaptically stored memories. Neuron **45**(4), 599–611 (2005)

[60] Päpper, M., Kempter, R., Leibold, C.: Synaptic tagging, evaluation of memories, and the distal reward problem. Learning & Memory **18**, 58–70 (2011)

[61] Benna, M.K., Fusi, S.: Computational principles of synaptic memory consolidation. Nature neuroscience **19**(12), 1697–1706 (2016)

[62] Luboeinski, J., Tetzlaff, C.: Organization and priming of long-term memory

representations with two-phase plasticity. Cognitive Computation (2022) https://doi.org/10.1007/s12559-022-10021-7

[63] Amit, D.J., Gutfreund, H., Sompolinsky, H.: Storing infinite numbers of patterns in a spin-glass model of neural networks. Physical Review Letters **55**(14), 1530 (1985)

[64] Luboeinski, J., Schmitt, S., Shafiee, S., Hater, T., Bösch, F., Tetzlaff, C.: Plastic Arbor: a modern simulation framework for synaptic plasticity – from single synapses to networks of morphological neurons. PLOS Computational Biology **22**(2), 1013926 (2026)

[65] Lehr, A.B., Luboeinski, J., Tetzlaff, C.: Neuromodulator-dependent synaptic tagging and capture retroactively controls neural coding in spiking neural networks. Scientific Reports **12**, 17772 (2022)

[66] Kastellakis, G., Silva, A.J., Poirazi, P.: Linking memories across time via neuronal and dendritic overlaps in model neurons with active dendrites. Cell Reports **17**(6), 1491–1504 (2016)

[67] Luboeinski, J., Tetzlaff, C.: Modeling emergent dynamics arising from synaptic tagging and capture at the network level. In: Sajikumar, S., Abel, T. (eds.) Synaptic Tagging and Capture: From Synapses to Behavior, 2nd edn., pp. 471–503. Springer, Cham, Switzerland (2024). Chap. 23. https://doi.org/10.1007/978-3-031-54864-2_23

[68] Kim, K., Lakhanpal, G., Lu, H., Khan, M., Suzuki, A., Kato Hayashi, M., Narayanan, R., Luyben, T., Matsuda, T., Nagai, T., Blanpied, T., Hayashi, Y., Okamoto, K.: A temporary gating of actin remodeling during synaptic plasticity consists of the interplay between the kinase and structural functions of camkii. Neuron **87**(4), 813–826 (2015) https://doi.org/10.1016/j.neuron.2015.07.023

[69] Fujii, H., Inoue, M., Okuno, H., Sano, Y., Takemoto-Kimura, S., Kitamura, K., Kano, M., Bito, H.: Nonlinear decoding and asymmetric representation of neuronal input information by camkiiα and calcineurin. Cell reports **3**(4), 978–987 (2013)

[70] Gerstner, W., Kistler, W.M.: Spiking Neuron Models, 1st edn. Cambridge University Press, Cambridge, UK (2002)

[71] Roth, A., Rossum, M.C.W.: Modeling synapses. In: De Schutter, E. (ed.) Computational Modeling Methods for Neuroscientists, 1st edn. MIT Press, Cambridge/MA, USA (2009). Chap. 6

[72] Lin, J.-W., Faber, D.S.: Modulation of synaptic delay during synaptic plasticity. Trends in Neurosciences **25**(9), 449–455 (2002)

[73] Kobayashi, R., Tsubo, Y., Shinomoto, S.: Made-to-order spiking neuron model equipped with a multi-timescale adaptive threshold. Frontiers in Computational Neuroscience **3**(9) (2009)

[74] Fonseca, R.: Activity-dependent actin dynamics are required for the maintenance of long-term plasticity and for synaptic capture. European Journal of Neuroscience **35**(2), 195–206 (2012)

[75] Szabó, E.C., Manguinhas, R., Fonseca, R.: The interplay between neuronal activity and actin dynamics mimic the setting of an ltd synaptic tag. Scientific reports **6**(1), 33685 (2016)

[76] Lee, S.-J.R., Escobedo-Lozoya, Y., Szatmari, E.M., Yasuda, R.: Activation of camkii in single dendritic spines during long-term potentiation. Nature **458**(7236), 299–304 (2009)

[77] Nogueira, F.: Bayesian Optimization: Open source constrained global optimization tool for Python (2014–). https://github.com/bayesian-optimization/BayesianOptimization

[78] Henley, J.M., Wilkinson, K.A.: Synaptic AMPA receptor composition in development, plasticity and disease. Nature Reviews Neuroscience **17**(6), 337–350 (2016)

[79] Akar, N.A., Biddiscombe, J., Cumming, B., Kabic, M., Karakasis, V., Klijn, W., Küsters, A., Peyser, A., Yates, S., Hater, T., Huisman, B., Hagen, E., Schepper, R.D., Linssen, C., Stoppels, H., Schmitt, S., Huber, F., Engelen, M., Bösch, F., Luboeinski, J., Frasch, S., Drescher, L., Landsmeer, L.: Arbor Library v0.9.0 (2023). https://doi.org/10.5281/zenodo.8233847